Chemical Engineering Journal 511 (2025) 161956

Contents lists available at ScienceDirect

Chemical Engineering Journal

journal homepage: www.elsevier.com/locate/cej

Manipulating plating mode of bimetallic Cu-Sn and Zn-Sn electrodes for electrochemical denitrification to gaseous nitrogen

Zhi-Lun Wu [a], Yu-Jen Shih [a,*], I-Hsuan Chen [a], Yi-Chun He [a], Chin-Pao Huang [b]

[a] Institute of Environmental Engineering, National Sun Yat-sen University, Taiwan
[b] Department of Civil and Environmental Engineering, University of Delaware, Newark, DE 19716, USA

ARTICLE INFO

Keywords:
Nitrate reduction
N_2 selectivity
Deoxygenation
Tin electrode
Passivation

ABSTRACT

Denitrification to gaseous N_2 is the best strategy for treating water samples with low nitrate contamination. Tin-based M − Sn electrodes exhibit high nitrate reduction rates with minimal ammonia production. M (Cu or Zn) and Sn metals serve as active sites for deoxygenation and hydrogenation reactions, respectively. This study synthesizes M − Sn bimetallic electrodes used for nitrate reduction reaction (NO_3^-RR). The layered plating sequence of metals critically influences nitrate reduction pathways and regulates N_2 selectivity. Both Cu and Zn metals can directly mediate the first electron transfer step through phase transformation, generating NH_3 and NO_2^- as predominant intermediates, respectively, at varying applied potentials. Sn coating enhances hydrogen (H•) adsorption on the Cu or Zn sublayer, increasing N_2 selectivity and faradaic efficiency to over 90 % at a working potential of −1.0 V (vs. RHE). Energy state calculations clarify that neighboring H on Sn domains lowers the barrier for adsorbed oxygenated nitrogen species on M metals. When Sn is plated as the top layer in Sn_1Cu_1 and Sn_1Zn_1 coatings, a consistently high N_2 selectivity and low electrical energy per order (EE/O < 0.25 kWh m^{-3}) are achieved during cycling electrolysis of real wastewater (NO_3^- ~ 500 mg-N L^{-1}, current density = 10 mA cm^{-2}).

1. Introduction

Nitrogen compounds, including nitrate (NO_3^-), nitrite (NO_2^-), ammonium (NH_4^+), gaseous N_2 and, organic nitrogen, are transported through the nitrogen cycle in natural environment [1]. Nitrogen species are regarded as macronutrients, but their excess, mainly from anthropogenic activities, will lead to eutrophication [2]. Due to their high solubility and widespread presence in water bodies, oxygenated nitrogen like NO_3^- and NO_2^- easily contaminates the surface water and groundwater through runoff and irrigation. NO_3^-/NO_2^- pose significant risks to ecosystems and human health. Excessive intake of NO_3^- can cause methemoglobinemia in infants, a condition resulting from hemoglobin oxidation, leading to reduced oxygen capacity in red blood cells [3]. Additionally, NO_2^- in foods has been associated with increased risks of cancer, diabetes, and miscarriage in pregnant women [4]. The USEPA has established a standard level of 10 mg-N L^{-1} and 1 mg-N L^{-1} for nitrate and nitrite, respectively, in drinking water [5].

Current treatment technologies for nitrate wastewaters include physical separation and biochemical reduction methods. Reverse osmosis (RO) is commonly used to recover the nitrate ions [6]; nevertheless, the high cost of selective membranes and the issue of fouling limit its application. Biological denitrification utilize denitrifying bacteria to reduce nitrate to gaseous N_2 in an anaerobic environment [7]. However, the microbial growth is slow, and less effective due to the large space required for the installation of active sludge systems. The electrochemical nitrate reduction reaction (NO_3^-RR) minimizes secondary waste since the only chemical reagents required are electrons, driven by a specific applied potential [8]. This method offers advantages such as environmental compatibility, energy efficiency, and cost-effectiveness. The selection of electrode materials that can effectively mediate electron transfer to different nitrogen species is essential for the success of treating various types of wastewaters [9]. NO_3^-RR has been explored as a potential alternative approach to the Haber–Bosch process for synthesizing NH_3 from nitrogen (N_2) reduction, as NH_3 emerges as an important carbon-free energy carrier [10]. However, the low nitrate concentrations (typically 10–100 s mg L^{-1}) in waste streams, like agricultural and municipal wastewater, combined with the presence of complex chemical matrices, can limit the feasibility of NH_3 or urea generation [11]. Additionally, challenges like low economic viability and overall environmental impacts constrain NO_3^-RR to NH_3

* Corresponding author.
E-mail address: yjshih@mail.nsysu.edu.tw (Y.-J. Shih).

https://doi.org/10.1016/j.cej.2025.161956
Received 15 January 2025; Received in revised form 3 March 2025; Accepted 23 March 2025
Available online 24 March 2025

applications. In the realm of environmental engineering, therefore, the nitrate reduction to the harmless nitrogen gas (N_2) is the most practical and sustainable pathway [12].

Accordingly, NO_3^-RR involves a sequence where NO_3^- is directly reduced to NO_2^-, followed by hydrogenation to species with lower oxidation states, such as NO, N_2O, N_2, NH_2OH, and NH_3 [13]. To enhance the reduction efficiency, a strategy of tuning two distinct adsorption sites, i.e., O-metal and H-metal, on electrodes is normally employed [14]. The selectivity of NO_3^- to either NH_3 or N_2 heavily depends on the strength of adsorbed H• on the metals [15]. In our previous work, Cu_2O-to-Cu transformation, particularly on Cu(111) facet, under cathode potential exhibited the excellent catalytic activity in NO_3^--to-NO_2^- step [16]. Other transition metals like Fe, Co, and Zn, which were relatively reductive than Cu, also possessed the cathode current densities in direct reduction at various potentials [17,18]. On the other hand, Sn is a non-noble metal catalyst effective in the hydrogenation step for perchlorate and carbon dioxide reduction. A $Pd_5Sn(200)_{95}$ electrode was previously synthesized for NO_3^-RR, with high N_2 selectivity of over 85 % [19].

During NO_3^-RR, surface Sn tended to passivate as hydroxides covering the Sn base. When a negative potential exceeding the redox potential between $Sn(OH)_{2(S)}$ and Sn was applied, solid-state diffusion of Sn into the bulk could lead to electroactivity loss [20]. Introducing a second noble metal, such as Pd and Pt [21], helped maintain H-enriched surfaces, preserving the integrity of the bimetallic electrode. On bimetallic M − Sn electrodes, transition metals, Cu or Zn, as M sites are hypothesized to act as primary mediators, where the phase transition of M (I)/(II) ⇌ M^0 governs the electron transfer from $NO_{2(ad)}^-$ to $NO_{2(ad)}^-$ [22–24]. Consequently, Sn passivation is mitigated during hydrogenation, facilitating the further reduction of oxygenated nitrogen to N_2. This study aims to tune the layered-plating mode on bimetallic electrodes to improve NO_3^-RR efficiency. The crystalline orientation of M and Sn is correlated with N_2 selectivity, as well as the faradaic efficiency and charge transfer kinetic. A real electroplating wastewater containing nitrate (with very dilute chloride concentration) is treated using constant current electrolysis, in which the durability of the M − Sn electrode is examined.

2. Materials and methods

2.1. Electroplating of M-Sn electrodes

Bimetallic M − Sn electrodes were fabricated using a layered-plating method with a Ni foam (NF 94 pore per inch, Innovation Materials Co., Ltd, Taiwan) as the substrate. An electroplating cell was assembled with an NF cathode and a commercial dimensionally stable anode (DSA, IrO_2/Ti). The pristine NF was initially soaked in acetone and H_2SO_4 for 1 h to remove the grease and other residues. Plating baths for Cu, Zn, and Sn were prepared using 0.05 M $CuCl_2$ (Honeywell) in H_3PO_4 (Honeywell), 0.05 M $ZnSO_4{\cdot}7H_2O$ (Thermo Scientific) in 0.1 M H_3BO_3 (J.T. Baker) and H_3PO_4, and 0.05 M $SnCl_2$ (Alfa Aesar) in H_2SO_4 (Honeywell), respectively. The pH of each plating solution was adjusted using respective phosphoric or sulfuric acid, and the plating temperature was maintained at 25 °C using a circulating water bath. 1-fold critical micelle concentration of BZT (1.78×10^{-3} M benzethonium chloride, $C_{27}H_{42}ClNO_2$, Sigma Aldrich) was added in each of plating baths as the modifier. The mode of metal deposition was adjusted by sequential electrolysis at a constant current density of 50 mA cm^{-2}, transferring the NF substrate between different bathes, as shown in Fig. 1; including Sn as the intermediate layer and M (Cu or Zn) as the surface layer: M_3Sn_1/NF, M_1Sn_1/NF, and M_1Sn_3/NF, and configurations with an intermediate M layer and Sn surface layer: Sn_3M_1/NF, Sn_1M_1/NF, and Sn_1M_3/NF. The subscript numbers represent the plating duration in minutes. Each layer of metal coating was rinsed with 0.1 M H_2SO_4 and deionized water in the ultrasonic batch, and the obtained bimetallic electrodes were dried in the vacuum before use.

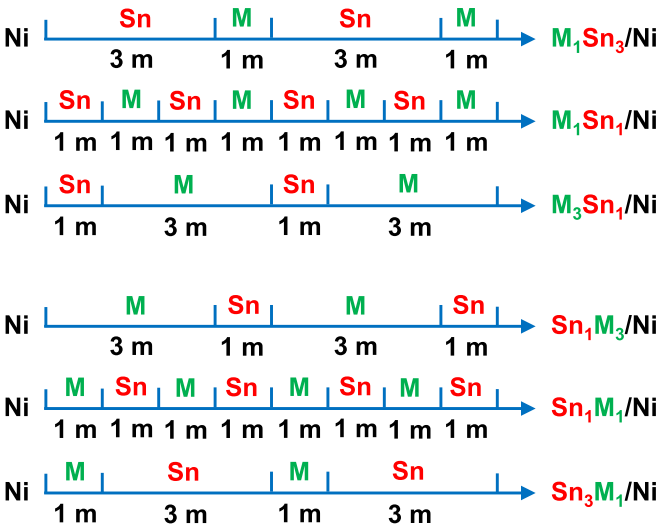

Fig. 1. Plating mode of layered M − Sn coatings (M = Cu or Zn) under applied current density of 50 mA cm^{-2} for different duration (min).

2.2. Nitrate electrolysis

The electrochemical characteristics and behavior of NO_3^-RR on M − Sn/NF electrodes were analyzed on a potentiostat (CHI611C, CH Instruments, Inc., Austin, TX, USA), with an Ag/AgCl (3 M NaCl) (E^0 = 0.195 V, RE-1B, ALS Co., Ltd) reference electrode and an IrO_2/Ti auxiliary electrode. All working potentials were corrected with respect to a reversible hydrogen electrode (RHE) by $E(\text{vs. RHE}) = E(\text{vs.Ag/AgCl}) + 0.059\text{pH} + E^0_{Ag/AgCl}$. NO_3^-RR using bimetallic electrodes was performed in a polymethylmethacrylate (PMMA) electrolytic cell with dimensions of 6 cm × 1 cm × 10 cm (in HLW). The nitrate solution was recirculated using peristaltic pumps at a flow rate of 3 mL s^{-1}. The Ag/AgCl reference was positioned between electrodes (effective area = 50 cm^2), with a 1 cm spacing, to control the working potential. During electrolysis, concentrations of nitrogen species were measured to calculate selectivity (S_N) and faradaic efficiency (FE_N),

$$S_N = \frac{[N]}{[NO_3^-]_0 - [NO_3^-]_t} \times 100 \quad (1)$$

$$FE_N(\%) = \frac{nF[N]V}{\int Idt} \times 100 \quad (2)$$

where n is the number of electrons, 2, 5, and 8 for NO_2^-, N_2, and NH_3, respectively; F is the Faraday constant (96485 C mol^{-1}), V is the solution volume (L), and [N] represents NO_2^--N, NH_3-N, and N_2-N in mol L^{-1}.

2.3. Analysis

An ion chromatography system (Eco IC 2.925.0020, Metrohm, USA) was used to measure NO_2^- and NO_3^- in the samples. The concentration of aqueous NH_4^+ was quantified using a flow injection analyzer (FIA, Lachat's Quik Chem 8500 Series 2, Loveland, Colorado, USA) based on the indophenol method at 630 nm (Method 350.1, USEPA). Other unstable and short-lived intermediates like NO_2, NO, N_2O, and NH_2OH were considered negligible. The concentration of N_2 was estimated by a mass balance relationship relative to the initial nitrate concentration, as follows: $[N_2\text{-N}] = [NO_3^-\text{-N}]_0 - [NO_3^-\text{-N}]_t - [NO_2^-\text{-N}] - [NH_4^+/NH_3\text{-N}]$. The morphology of metal coatings was observed using a scanning electron microscope (JSM-6700F, JEOL, Tokyo, Japan), with energy dispersive spectroscopy (EDS, INCA400, Oxford,UK) for elemental analysis. Grazing incidence X-ray diffraction (GID-XRD, D2 PHASER, Bruker Co., USA) with a Cu Kα source (λ = 1.5406 Å) was used to determine the crystal

structure at a scan rate of 0.06∘ s^{-1} and incidence angle 2θ of 20–85°. Chemical states were specified by X-ray photoelectron spectroscopy (XPS, PHI 5000 VersaProbe, Physical Electronics, Inc., USA) with a Al Kα X-ray source (1487 eV). An operando Raman spectrometer (MRID model, ProTrusTech, Taiwan) (emitting radiation λ = 785 nm) was employed to analyze changes in chemical bond modes within the metal coatings during voltammetry scanned in specific potentials.

3. Results and discussion

3.1. Characterization

SEM images of the electroplated metals are shown in Fig. S1, which reveals distinct morphologies, including angular, polyhedral, and flaky crystals for Sn, Cu, and Zn, respectively. The addition of a BZT surfactant has been found to modify loosely bound coatings of Sn into regular crystallites [25]. A cubic habit, enclosed with Sn{100} and Sn{111} facets, was shown to favor N_2 formation in NO_3^-RR process. In the bimetallic electrodes, the crystal shapes of both M and Sn were significantly altered compared to their individual morphologies. The intermediate metal layer undergoes moderate dissolution and co-deposition during the sequential plating of the surface metal layer in different baths. Fig. 2a-2c indicate the increasing size of Cu octahedrons as the plating time of Cu increases from Cu_1Sn_3 to Cu_3Sn_1, in which Sn recrystallizes into fine grains that are uniformly embedded within sublayer texture. When plating Sn over a Cu base layer, recrystallization leads to the formation of Sn nanoclusters growing along the edges and boundaries of the Cu polyhedrons, as shown in Fig. 2d-2f. The size of the Cu crystals decreases with increasing Sn plating time, from Sn_1Cu_3 to Sn_3Cu_1. In comparison to the flaky morphology of Zn, the deposition of Zn forms irregular sheets, covering the angular Sn base. The size of these Zn sheets increases with extended plating time, from Zn_1Sn_3 to Zn_3Sn_1, as shown in Fig. 2g-2i. Conversely, the flaky Zn crystals persist, while Sn precipitates as nano-flowers on the surfaces of Zn. The amount of Sn also increases with time, as illustrated from Sn_1Zn_3 to Sn_3Zn_1 in Fig. 2j-2 l.

XRD analyses in Fig. 3a evidence the presence of metallic crystals plated onto the Ni foam. The Sn layer is identified as β-Sn phase (tetragonal, I41/amd, #86–2265) by four peaks at 2θ of 30.6°, 32°, 43.9°, and 44.9°, corresponding to (200), (101), (220), and (211) crystal planes, respectively [26]. The Cu phase (cubic, Fm $\bar{3}$ m, #85–1326) is determined by peaks at 2θ of 43.3°, 50.4°, and 74.1°, representing (111), (200), and (220) planes, respectively [27]. Additionally, three primary peaks at 2θ of 36.2°, 38.9°, and 43.2° due to diffraction in (002), (100), and (101) planes, respectively, indicates a hexagonal lattice (P63/mmc, 87–0713) of Zn metal [28]. These well-defined crystal structures indicate that the last plated metal forms distinct crystallites on the underlying metal sublayer. The crystalline size (D_S) of the metals in the bimetallic M − Sn coatings are measured using a Scherrer equation ($D_S = \frac{K\lambda}{B\cos\theta}$), where K is the shape factor, λ is the wavelength of incident X-ray (1.5406 Å for Cu Kα), and B is the full width at half maximum for specific diffraction planes, as shown in Fig. 3b. Extending the plating time increases the grain size of surface metal (Cu or Zn) while decreasing that of the base Sn metal, aligning with the crystal growth observed through SEM analysis. This variation in crystal size also suggests recrystallization during the layered-plating process, in which galvanic deposition impacts the solubility of the sublayer [29]. Fig. 3c presents ratios of the primary facets of metals on M − Sn electrodes, i.e., $F_{Sn(200)} = \frac{I_{Sn(200)}}{I_{Sn(200)}+I_{Sn(101)}}$, $F_{Cu(111)} = \frac{I_{Cu(111)}}{I_{Cu(111)}+I_{Cu(200)}}$, $F_{Zn(002)} = \frac{I_{Zn(002)}}{I_{Zn(002)}+I_{Zn(101)}}$. The preference in crystal facet orientation is related to surface energy, with the morphology of metal particles largely determined by low-energy planes. Consequently, the surfaces of these metals are expected to be capped by the BZT additive during the plating process. Notably, single-crystal electrodes with lower Miller indices exhibit more regular surface structures. The F values of the metals tend to decrease with extended plating duration, indicating a decrease in crystal uniformity as the surface metal is repeatedly plated onto the base metal.

Effects of the plating mode on the chemical states of metals in the M − Sn electrodes are evaluated using XPS analysis, as shown in Fig. 3d-3f. Sn orbitals consist of $3d_{5/2}$ and $3d_{3/2}$ bands at binding energies of 486 eV and 495 eV, respectively. The $3d_{5/2}$ band in the Sn base can be deconvoluted into approximately 60 % zero valent Sn(0) and 40 % Sn(II) at 485.2 eV and 486.5 eV, respectively [30], indicating partial oxidation due to atmospheric exposure: $SnO + 2H^+ + 2e^- \rightleftharpoons Sn^0 + H_2O$ (E^0 = -0.084 eV vs. RHE); $O_2 + 2Sn^0 \rightarrow 2SnO$ (ΔG^0 = -510 kJ mol^{-1}). The characteristic peaks at their respective binding energies were further deconvoluted to determine the ratios of different chemical states, as summarized in Fig. 3g. During the layered-plating process in bimetallic electrodes, the Sn state undergoes oxidation to varying extents. The shift of the Sn^0 band toward Sn(II) is more pronounced in Cu-Sn than in Zn-Sn electrodes, which is ascribed to the higher reduction potential of Cu compared to Zn: $Cu_2O + 2H^+ + 2e^- \rightleftharpoons 2Cu^0 + H_2O$ (E^0 = 0.46 V) and

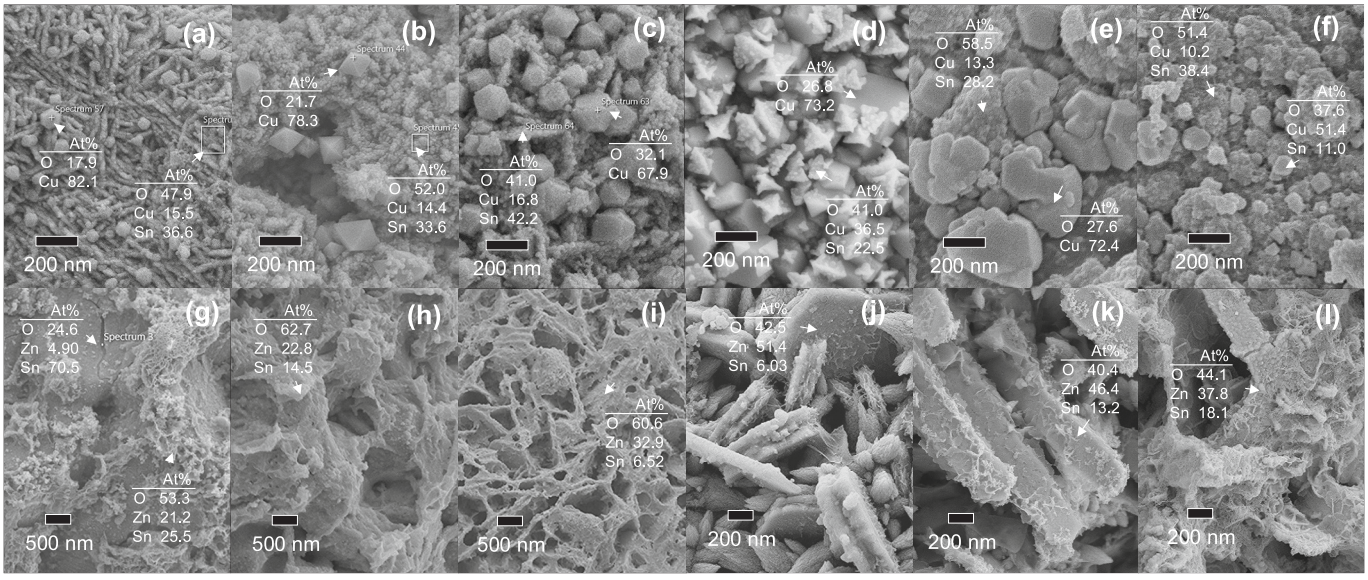

Fig. 2. SEM images of bimetal coatings: (a) Cu_1Sn_3, (b) Cu_1Sn_1, (c) Cu_3Sn_1, (d) Sn_1Cu_3, (e) Sn_1Cu_1, (f) Sn_3Cu_1, (g) Zn_1Sn_3, (h) Zn_1Sn_1, (i) Zn_3Sn_1, (j) Sn_1Zn_3, (k) Sn_1Zn_1, (l) Sn_3Zn_1.

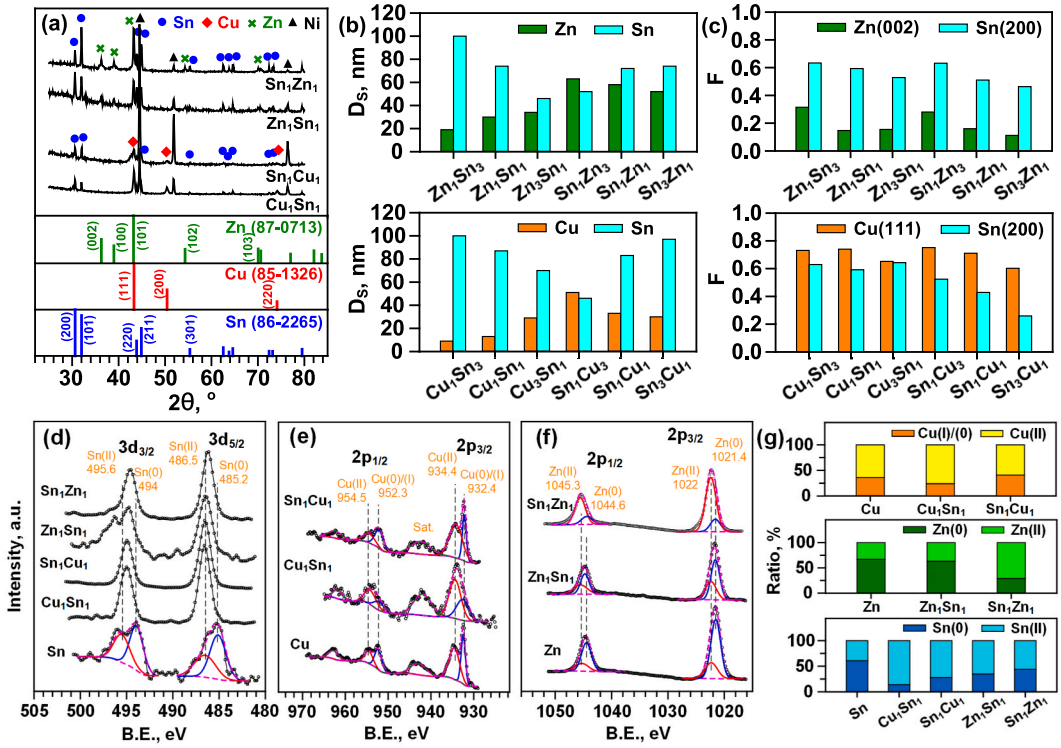

Fig. 3. (a) XRD pattern of M − Sn bimetallic electrodes with (b) corresponding crystalline sizes and (c) facet ratios as affected by plating mode. XPS analysis of (d) Sn 3d, (e) Cu 2p, and (f) Zn 2p orbitals. (g) Summary of chemical state ratios in metal coatings.

$ZnO + 2H^+ + 2e^- \rightleftharpoons Zn^0 + H_2O$ (E^0 = -0.43 V). The XPS spectra of Cu exhibit the $2p_{3/2}$ and $2p_{1/2}$ bands corresponding to the Cu(0)/Cu(I) state at 932.4 eV and 952.3 eV, respectively, along with the Cu(II) state at 934.4 eV and 954.5 eV, respectively [31]. Cu tends to oxidize when plated as the surface layer in Cu_1Sn_1, compared to the monometal Cu electrode. However, when Cu is plated as an intermediate layer in Sn_1Cu_1, the relatively reductive Sn deposition mitigates the oxidation of Cu state. In contrast, the reductive zero-valent Zn(0) (with $2p_{3/2}$ and $2p_{1/2}$ bands at 1021.4 eV and 1044.6 eV, respectively [32]) protects Sn from galvanic oxidation but transforms more to Zn(II) (1022 eV and 1045.3 eV) in the Sn_1Zn_1 coating.

3.2. Electrochemical behaviors

Fig. S2 illustrates the effect of nitrate addition on the voltammetry response using Sn, Cu, and Zn electrodes. In the background electrolyte (0.1 M Na_2SO_4, uncontrolled pH), the monometals exhibit reversible peak current densities, which are attributed to the redox reactions of the transition metals during voltammetric scans. These phase transformations correspond to the reduction of SnO to Sn, Cu_2O to Cu, and ZnO to Zn at peak potentials of approximately −0.85 V, −0.6 V, and −1.2 V (vs. RHE), respectively [21]. The variation in the peak potential of R_M (M = Sn, Cu, and Zn) also indicates the differing reductive characteristics of these metals. With the addition of nitrate (15 mM), a sharp increment in cathode current (R_N) is observed as the scanning potential surpasses R_M peak on Cu and Zn metal. However, this nitrate concentration-dependent current is negligible on Sn metal. This observation indicates that the first $2e^-$ transfer in nitrate conversion to nitrite occurs directly through phase transformation of R_M step (eq. (3)——5) on Cu and Zn [33,34].

$$M + NO_3^- \rightarrow M(NO_3^-) \quad (3)$$

$$M(NO_3^-) \rightarrow MO(NO_2^-) \quad (4)$$

$$MO + 2H^+ + 2e^- \rightarrow M + H_2O \ (R_M,\ M = Cu \text{ and } Zn) \quad (5)$$

Subsequent hydrogenation reduces the nitrogen species to lower oxidation states on R_N [35].

$$M + H^+ + e^- \rightarrow M(H\bullet) \quad (6)$$

$$M(H\bullet) + MO(NO_2^-) \rightarrow MO + \text{product } (R_N) \quad (7)$$

The absence of direct electron transfer on Sn suggests that nitrate is not reduced via the R_M mechanism but instead by indirect hydrogenation process (eq. (6) and (7). The electroanalysis of the Cu-Sn and Zn-Sn coatings with various metal ratios is present in Fig. 4a-4c and Fig. 4d-4f, respectively. Increasing the coverage of the M sublayer from Sn_3M_1 to Sn_1M_3 significantly enhances the current densities of R_N. Note that Sn alone cannot induce direct electron transfer for nitrate (Fig. S2a). Howeve, while integrated onto M (Cu or Zn) bases, R_N becomes concentration-dependent, underscoring the synergistic effects of the bimetallic composition on the NO_3^-RR pathways. The Cu or Zn base acts as nucleation sites for Sn crystallite growth, effectively regulating the electrodeposition, and vice versa. As a result, the Faradaic current associated with direct nitrate reduction is amplified on bimetallic electrodes compared to the Sn monometal electrode.

The electrode kinetics of R_N step are further evaluated using Nicholson and Shain theory [36]:

$$E_P = E^{0'} - \frac{RT}{\alpha n F}\left[0.78 + \ln\left(\frac{D_0^{1/2}}{k^0}\right) + \ln\left(\frac{\alpha n F}{RT}\nu\right)^{1/2}\right] \quad (8)$$

which predicts the heterogeneous rate constant, k^0 (cm s^{-1}), through the shift in the peak potential, E_P, of R_N with respect to the square root of the scan rate, $v^{1/2}$ (V s^{-1}). When the transfer coefficient $\alpha = \frac{1.86RT}{nF\left|E_P - E_{P/2}\right|}$ and the diffusion coefficient of nitrate ion D_0 (2×10^{-6} cm^2 s^{-1}) are given, this calculation simplifies to: $k^0(25^\circ C) = \frac{1.11 D_0^{1/2} v^{1/2}}{\left(E_P - E_{P/2}\right)^{1/2}}$, which is used to diagnose irreversibly diffusion-controlled behaviors [37]. Fig. 4g and Fig. 4h demonstrate the voltammetry for Cu and Zn electrode, respectively, in 15 mM NO_3^-, with the inset displaying the k^0 values obtained by

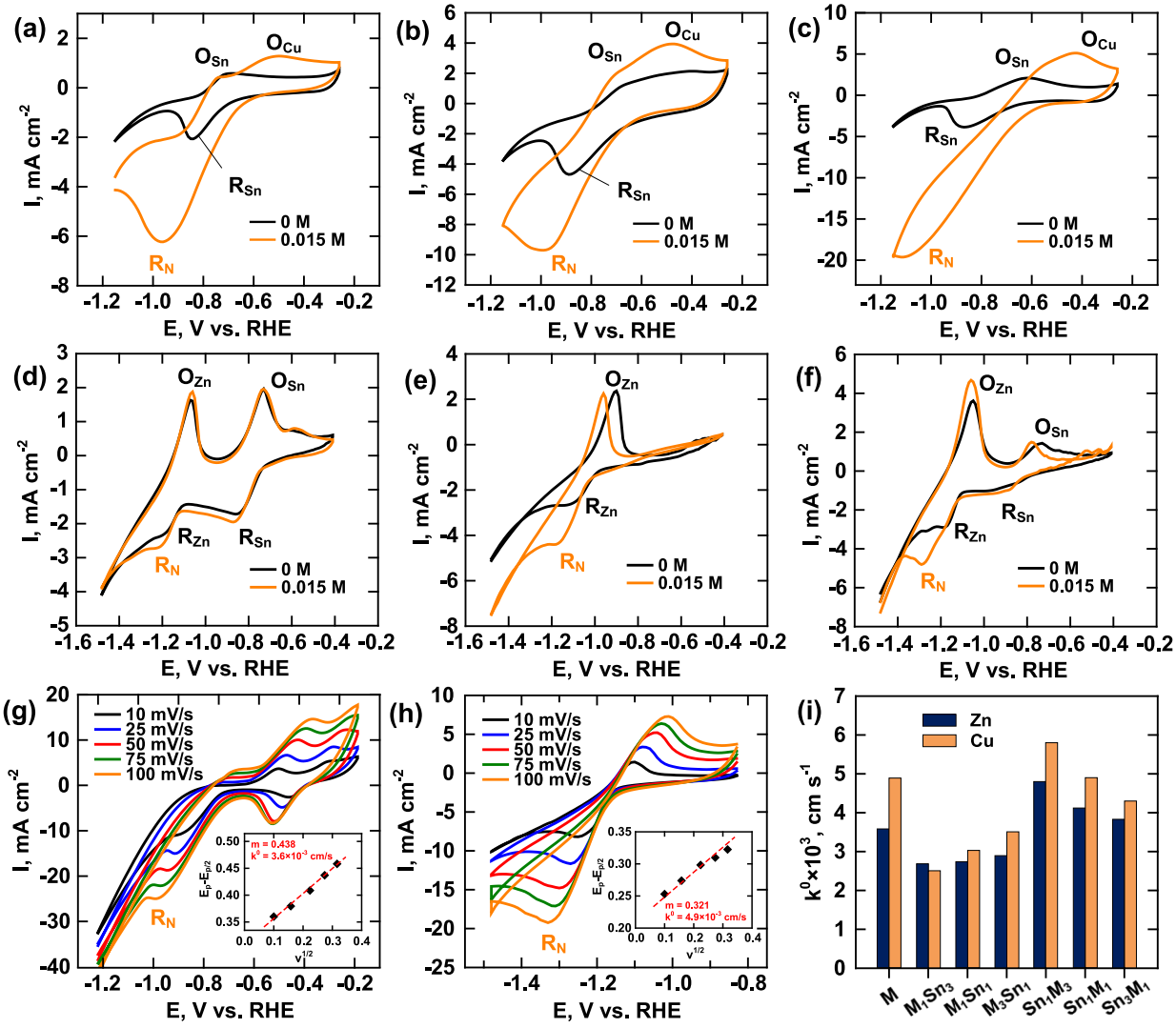

Fig. 4. Voltammetry analysis of (a) Sn_3Cu_1, (b) Sn_1Cu_1, (c) Sn_1Cu_3, (d) Sn_3Zn_1, (e) Sn_1Zn_1, and (f) Sn_1Zn_3 in the presence of 0.1 M Na_2SO_4, compared to those with addition of 15 mM NO_3^-. Effect of scan rate on voltammetry of (g) Sn_1Cu_1 and (h) Sn_1Zn_1 electrodes, and the effect of plating mode on heterogeneous rate constants (k^0).

linearly correlating the peak potential of R_N to $v^{1/2}$. The k^0 values of Cu- or Zn-based electrodes are generally higher than those of Sn-based electrodes, as shown in Fig. 4i. Furthermore, the k^0 values of Cu-Sn electrodes are consistently larger than those for Zn-Sn electrodes. Here, k^0 represents the rate of reducing adsorbed NO_3^-, with R_N considered the rate-determining step. This result confirms that Cu and Zn act as O-metals in the bimetallic electrodes, with Cu being more effective than Zn in the step of NO_3^- reduction to NO_2^-. When Sn, serving as the hydrogenation sites, is well-decorated on Cu or Zn base, the H-enriched surfaces significantly accelerate the NO_3^-RR rate.

To better understand the charge transfer efficiency of NO_3^-RR on bimetal electrodes, the electrochemical impedances are analyzed (−1.0 V vs. RHE, 0.1 M NO_3^-). As displayed in Fig. 5a, the Nyquist plots are modeled using the inset equivalent circuit, which comprises series components of electrical double layer (EDL) capacitance (C_{dl}) and charge transfer resistance (R_{CT}) in parallel, coupled with the capacitance (C_S) and resistance (R_L) of metal-electrolyte interface [38]. (EIS parameters obtained by fitting the model are listed in Table S1.) Notably, the semicircles observed on Cu-Sn electrodes are smaller compared to those of Zn-Sn, signifying faster charge transfer-controlled kinetics at Cu sites than at Zn sites [39]. Voltammetry analysis in Fig. 5b, conducted by scanning potentials in the supporting electrolyte (0.1 M Na_2SO_4, v = 0.01 V s^{-1}), reveals the redox behavior of the metal transformation. These basic current densities arise from electrical charging/discharging reactions, which vary depending on the plating mode. The double-layer capacitance (C_{dl}) in the non-Faradaic region was estimated using the equation: $C_{dl} = \frac{d\sigma_{+/-}}{dE} = \frac{I_a - I_c}{v}$ (where $\sigma_{+/-}$ is the surface charge in coulomb, I_a and I_c are the charging currents). This estimation provides a measure of the electrochemical surface area [40]. Fig. 5c compiles the R_{CT} and C_{dl} values, showing a general trend where the effective sites of the bimetallic electrodes increase when Sn is plated as the surface layer compared to when it is the sublayer. Additionally, the decrease in R_{CT} values alongside an increase in C_{dl} suggests that the enhanced rate of electro transfer is associated with the extended surface area. However, despite having smaller C_{dl}, the Cu-Sn combinations exhibit significantly lower R_{CT} values than those of Zn-Sn, which is consistent with the calculated heterogeneous rate constants shown in Fig. 4i.

The cathode polarization curves of Sn, Cu, and Zn electrodes in the electrolyte are analyzed to assess the catalytic reactivity of the metals in the hydrogenation process, as shown in Fig. S3a. The onset of hydrogen evolution reaction (HER) occurs at −0.7 V and −0.8 V (vs. RHE) for Cu and Sn monometals, respectively, which are lower than that for Zn (−1.1 V). Namely, Zn initiates H_2 generation at more negative potentials. The electrochemical pathways of HER can be divided into a Volmer

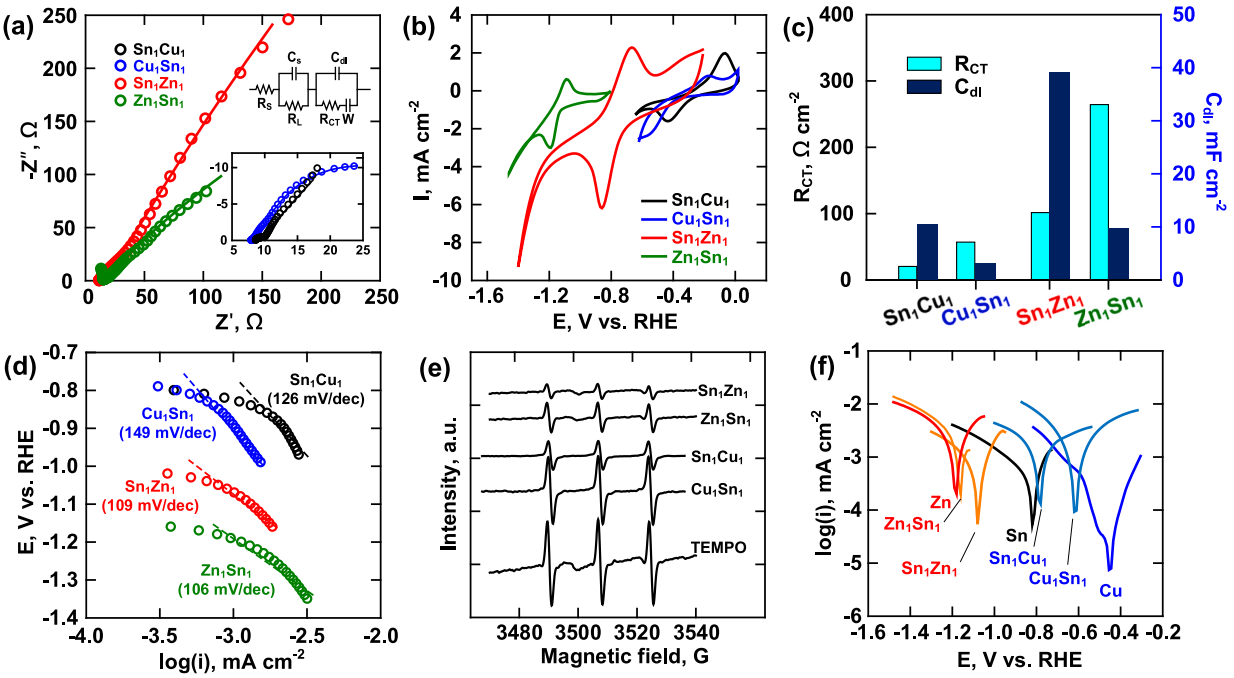

Fig. 5. (a) Impedance analysis, (b) voltammetry, and (c) the corresponding charge transfer resistance and double-layer capacitance. (d) Polarization at hydrogen evolution potentials, (e) EPR spectra of TEMPO-H, and (f) Tafel plots for corrosion behaviors on M − Sn electrodes.

step, which transfers the first electron to form adsorbed H•, followed by a Heyrovský step, where H_2 is produced from the second electron in the combination with H• [41].

$$M + H^+ + e^- \rightarrow M - H\bullet \text{ (Volmer step)} \quad (9)$$

$$M - H\bullet + H^+ + e^- \rightarrow M + H_2\uparrow \text{ (Heyrovský step)} \quad (10)$$

The descending order of the Tafel slopes is Sn (160 mV dec^{-1}) > Cu (118 mV dec^{-1}) > Zn (106 mV dec^{-1}), as shown in Fig. S3b. A Tafel slope close to 120 mV dec^{-1} suggests that the Heyrovský step is rate-determining in this HER model. As a result, among the metals Zn exhibits the fastest hydrogenation kinetics but requires a higher overpotential for H_2 evolution. Fig. 5d presents the Tafel plots of bimetallic M − Sn electrodes, showing varying slopes according to different layered-plating modes, following Cu_1Sn_1 (149 mV dec^{-1}) > Sn_1Cu_1 (126 mV dec^{-1}) > Sn_1Zn_1 (109 mV dec^{-1}) ~ Zn_1Sn_1 (106 mV dec^{-1}). The Zn-Sn composites demonstrate high reactivity in the hydrogenation step. The free energy of H adsorption (ΔG_H) on Sn has been reported to fall on the left of the volcano plot [42]. In other words, Sn binds the H^+ too strongly, which hinders the release of H_2 [43]. It was found that incorporating an appropriate amount of Sn in bimetal composites increased the energy barrier of HER [44]. Therefore, Zn-Sn coatings in bimetallic electrodes increase HER overpotential, while maintaining surfaces stably enriched with adsorbed H•. The EPR spectra of 1 mg L^{-1} 2,2,6,6-tetramethylpiperidine-1-oxyl (TEMPO), used as a hydrogen trapper, are shown in Fig. 5e. TEMPO, a nitroxyl radical, weakens upon hydrogenation to TEMPOH, thus serving a probe for the presence of H• [45]. During electrolysis under an applied current of 20 mA cm^{-2}, electrodes with Sn as the surface layer, such as Sn_1Cu_1 and Sn_1Zn_1, display lower EPR intensities compared to those where Sn is the base metal, i.e., Cu_1Sn_1 and Zn_1Sn_1. In addition, the minimal change in the TEMPO signal on Cu_1Sn_1 implies the limited hydrogenation on Cu metal. Voltammetry results have confirmed that Sn primarily conducted HER in the presence of NO_3^-. These findings suggest that in M − Sn composites, NO_3^- ions are preferentially adsorbed on M sites, while H^+ are adsorbed on Sn sites. The division of adsorption sites enhance the nitrate reduction efficiency as a result of collaborative interactions between the two metals.

Faradaic currents by NO_3^-RR involve reversible phase transitions of Cu and Zn, where the passivated films must resist corrosion when facilitating direct electron transfer. The Tafel plots in Fig. 5f highlight the corrosion potential (E_{corr}) of M − Sn electrodes in 15 mM NO_3^-, which follows the order: Cu (−0.45 V) > Sn (−0.82 V) > Zn (−1.17 V). As a result, Cu is the most resistant metal in reducing NO_3^-. In bimetallic electrodes, plating a more oxidative metal on the base metal shifts E_{corr} to less negative values. This means that, under cathode potential close to E_{corr}, the surface metal with an increased E_{corr} is reduced first, acting as an electron donor to stabilize the overall bimetal coating during NO_3^-RR [46]. Therefore, the surface metals shield the underlying layers, thus enhancing the electrode's resistance to nitrate-induced corrosion.

3.3. Electrochemical NO_3^- Reduction

Effects of working potentials (vs. RHE) on NO_3^-RR using M − Sn electrodes are present in Fig. 6a and 6b, in terms of selectivity (S_N), removal efficiency (R), and faradaic efficiency (FE) (NO_3^- = 100 mg-N L^{-1}). Electrolysis was performed in chronoamperometry mode within a potential range of −0.6 V to −1.6 V. Voltammetry analysis (Fig. 4) has revealed phase transitions of Cu and Zn metals at varied potentials, enabling the first $2e^-$ transfer for reducing nitrate on these bimetallic electrodes. On Cu_1Sn_1, R and FE reach 68 % and 75 %, respectively, at −1.0 V, where S_{N2} is maximized at 84 %. Increasing applied potential further elevates NH_3 yield but significantly decrease FE, likely due to concurrent hydrogen evolution reaction (HER) [47]. Conversely, Zn_1Sn_1 achieves the highest S_{N2} of 76 % at −1.2 V, corresponding to R of 64 % and FE of 71 %. However, at lower potentials, a notable amount of nitrite (S_{NO2-} > 50 %) is observed, suggesting its lower hydrogenation capability for adsorbed nitrite species, compared to Cu_1Sn_1. This result aligns with the high overpotential required for HER on M − Zn electrodes (Fig. 5d), which overlaps with potentials for nitrate reduction (Fig. 4e). Fig. 6c and 6d illustrate the effects of plating modes on NO_3^-RR using Cu-Sn (at −1.0 V) and Zn-Sn (at −1.2 V) electrodes, respectively. Typically, Cu and Zn as surface metals on the Sn base layer produce more NH_3 and NO_2^-, respectively, compared to those electrodes with a surface Sn layer on Cu and Zn bases. The increased selectivity for NH_3 and NO_2^- with longer plating times of Cu and Zn on Sn metal explains the

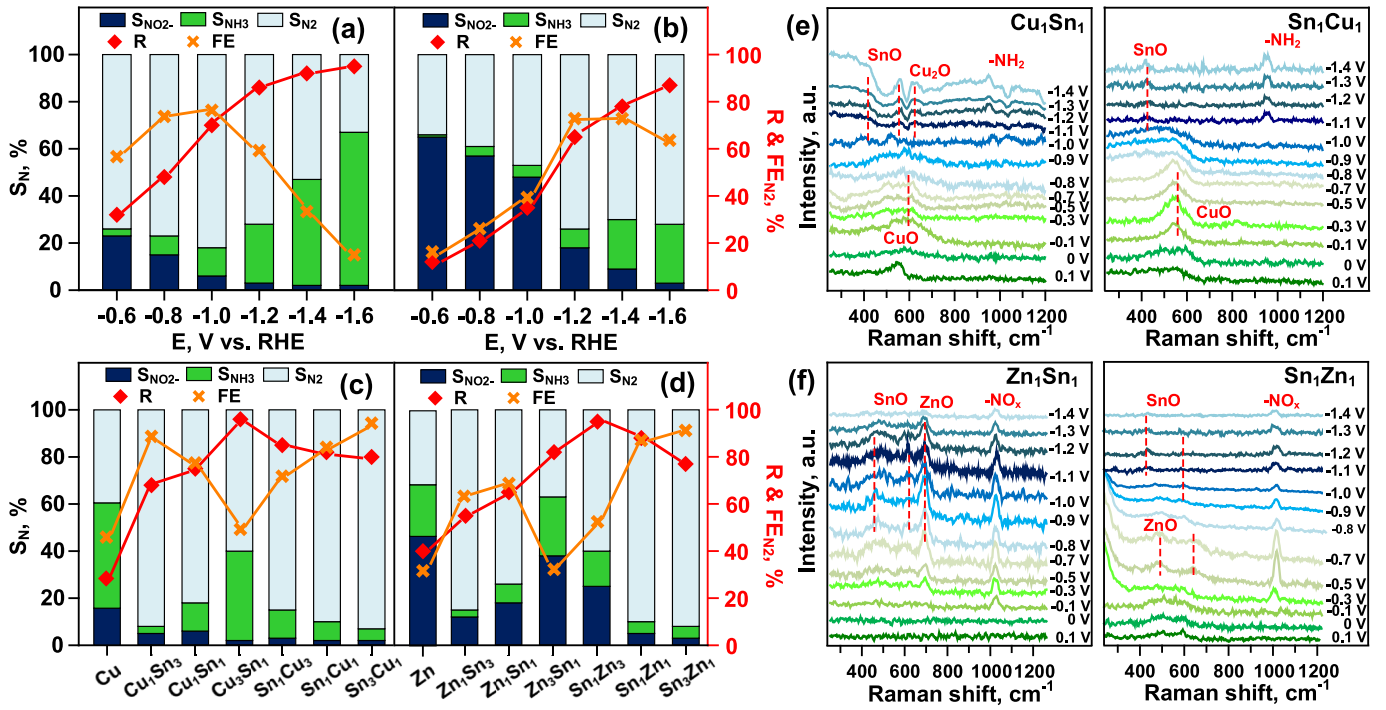

Fig. 6. Effects of applied potential (vs. RHE) at (a) Cu_1Sn_1 and (b) Zn_1Sn_1, and plating mode of (c) Cu-Sn and (d) Zn-Sn electrodes on the performance of NO_3^-RR (initial NO_3^- = 100 mg-N L^{-1}, 0.1 M Na_2SO_4; S_N: selectivity, R: removal efficiency, FE: faradaic efficiency). Operando Raman spectroscopy during electrochemical NO_3^- reduction at (e) Cu-Sn and (f) Zn-Sn electrodes (0.1 M NO_3^-).

strong influence of surface metal composition on the preferred byproducts. The monometallic Cu and Zn coatings, included for comparison, exhibit average R and FE values below 40 %, clarifying the synergistic effect of bimetallic coatings. Thermodynamically, NO_3^-RR pathways involved concurrent deoxygenation and hydrogenation processes, where the two end products, N_2 and NH_3, compete with each other.

$$NO_3^- + 2H^+ + 2e^- \rightleftharpoons NO_2^- + H_2O \quad (11a)$$

$$2NO_2^- + 8H^+ + 6e^- \rightleftharpoons N_2 + 4H_2O \quad (11b)$$

$$NO_2^- + 7H^+ + 6e^- \rightleftharpoons NH_3 + 2H_2O \quad (11c)$$

On monometallic electrodes, the metal state shall be responsible for mediating electron transfer to adsorbed nitrogen and hydrogen species. Hence, the bond strength between metal sites and NO_3^-/H^+ ions critically determines the reaction pathways. Cu is considered the most effective for nitrate adsorption due to its unpaired d-electrons, which have a d-band configuration similar to the π* orbital in the LUMO of NO_3^- [47]. This electronic similarity favors ammonia production at high applied potentials. By contrast, zero-valent Zn, despite its high reduction potential, is easily oxidized to ZnO, making subsequent reduction of nitrite to the lowest-oxidation state of ammonia sluggish [48]. Nevertheless, both N_2 formation and NO_3^- removal efficiency improve on Sn_1Cu_1 (R = 82 %, S_{N2} = 90 %) and Sn_1Zn_1 (R = 88 %, S_{N2} = 92 %). This outcome indicates that incorporating H-metal, i.e., Sn, enriches reactive H• over electrode surfaces, promoting the conversion of nitrogen intermediates to N_2. In other words, the trapping of H• on Sn results in hydride functional groups, which modulate hydrogenation reactions at Cu and Zn sites. The metal phase transition on Cu-Sn and Zn-Sn electrodes during NO_3^- electrolysis is observed on operando Raman spectra as shown in Fig. 6e and Fig. 6f, respectively. At cathode potentials, the shift of vibrational modes in the 500 – 650 cm^{-1} region (F_{2g} and E_g modes) indicates the gradual reduction of CuO to Cu_2O. On Cu_1Sn_1, a steady-state cuprous film forms in conjunction with SnO at potentials more negative than −1.0 V, correlating with the rocking mode of ρ NH_2 (960 cm^{-1}) [49], an intermediate for NH_3 production. The formation of SnO suggests moderate passivation of the Sn metal layer due to hydrogenation reactions, as evidenced by the vibrations of E_g and A_{1g} modes in the 450 – 600 cm^{-1} range [50]. On Sn_1Cu_1, the signal for CuO-to-Cu_2O transformation at 550 cm^{-1} is notably weakened. On the other hand, on Zn_1Sn_1, Raman bands at 460 cm^{-1} and 639 cm^{-1} correspond to the transverse and longitudinal phonon modes (E_1) of ZnO, respectively [51]. A vibrational band at 1030 cm^{-1} found on Zn-Sn electrodes is attributed to the accumulation of adsorbed oxygenated nitrogen (NO_x) [52] at potentials up to −0.1 V. Metal passivation is also mitigated on Sn_1Zn_1, where the nitrate/nitrite predominate as surface-adsorbed species over a wide potential range. The M − O vibration modes on monometallic electrodes in Fig. S4 intensify with increasing cathode potentials in Na_2SO_4 electrolyte, reflecting the redox behavior of metal surfaces upon hydrogenation. With the addition of nitrate, variations in functional nitrogen species, such as NH_2 and NO_x, influence the Raman shifts of metal oxides, providing insights into NO_3^-RR selectivity. These findings confirm the role of bimetallic coatings in determining nitrate conversion pathways, i.e., to NH_3 and NO_2^- on Cu-Sn and Zn-Sn composites, respectively.

The density function theory (DFT) program was performed using Forcite modules [53] to evaluate the adsorption energy (E_{ads}) of nitrogen and hydrogen species over various M − Sn surface combinations. Detailed computational methods are provided in the supporting information, where E_{ads} is defined as the difference between the energy of the adsorbed molecule and the sum of the energies of the clean surfaces and the gas-phase species [54]. Hydrogenation steps involve interactions between NO_3^- and H^+ on two metal sites, M_1/M_2, which can include Cu/Sn, Sn/Cu, Zn/Sn, and Sn/Zn pairs.

$$E_{ads,NO_3} = E_{M_1,NO_3^-} - E_{M_1} - E_{NO_3^-} (NO_3^- \text{ on M1 site}) \quad (12)$$

$$E_{ads,H} = E_{M_2,H^+} - E_{M_2} - E_{H^+} (H^+ \text{ on } M_2 \text{ site}) \quad (13)$$

Fig. 7a presents the free energy of H on bridge sites of various metal crystal facets. Across monometallic surfaces, Sn(2 0 0) exhibits strongest

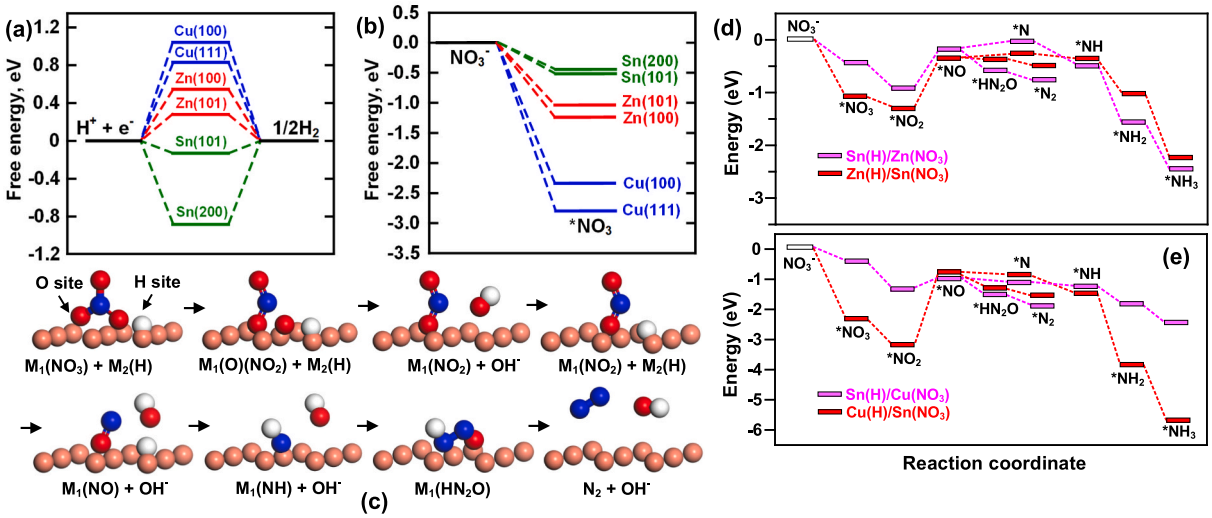

Fig. 7. (a) DFT simulation of free energies for (a) hydrogenation and (b) nitrate adsorption on Sn, Cu, and Zn monometal electrodes. (c) Mechanism of nitrate reduction on bimetal sites, and free energy change for each intermediate on (d) Zn-Sn and (c) Cu-Sn electrodes, by varying metals responsible for H and O adsorption sites.

hydrogen binding due to its highly negative E_{ads}. The predominance of Sn(1 0 1) increases when it is plated as the surface layer on Sn_1Zn and Sn_1Cu_1, compared to those with Sn as the sublayer, as determined by the diffractometer in Fig. 3c, implying a reduced energy barrier for H_2 evolution. NO_3 adsorption on different facets of monometals is modeled as shown in Fig. 7b, where the binding energies of nitrate on Cu facets exhibit much stronger interactions compared to Zn and Sn. Strong adsorption of NO_3^- is expected to lower the energy state of the first discharge step: $* + NO_3^- \rightarrow *NO_3 + e^-$ [55]. After the first deoxygenation on the M_1 site (the O-bonded metal), the reaction proceeds as:

$$M_1(NO_3^-) \rightarrow M_1(O)(NO_2^-) \quad (14)$$

Hydrogenation begins with the interaction between the adsorbed NO_2^- and H.

$$M_1(O)(NO_2^-) + M_2(H) \rightarrow M_1(NO_2) + 2M_2 + OH^- \quad (15)$$

Intermediates, including $*NO_2$, *NO, and $*HN_2O$, adsorbed on M_1 site are reduced by the *H on M_2 site, ultimately forming N_2 as the final product [56]. The NO_3^-RR pathway leading to N_2 is visualized in Fig. 7c. Alternatively, $*NO_2$ may undergo a parallel reduction sequence via *N, *NH, $*NH_2$, and $*NH_3$. The final step involves NH_3 desorption from the catalyst surface [57]. The calculated energy states of each intermediate in these reaction steps are summarized in Table S2, with optimized adsorption geometries shown in Fig. S5. Fig. 7d and 7e depict the energy profiles of NO_3^-RR to N_2 and NH_3 on different metal combinations, where Zn or Cu and Sn alternatively function as M_1 and M_2 sites for NO_3^- and H^+ adsorption, respectively. Notably, the predominant facets of Cu(1 1 1), Zn(1 0 1), and Sn(1 0 1) were selected for these computations, based on XRD analysis in Fig. 3. It is clear that the free energies for the conversion of NO_3^- to $*NO_3$ on M(H)/Sn(NO_3) are much lower than on Sn(H)/M(NO_3). However, the deoxygenation of $*NO_3$/$*NO_2$ to *NO on M(H)/Sn(NO_3) goes through an uphill with larger energy barriers than on Sn(H)/M(NO_3). This finding indicates that the adsorption strength of nitrate/nitrite on M site weakens as a second Sn metal is responsible for H adsorption. Additionally, $*NO_2$ exhibits lower energies on Cu-Sn than on Zn-Sn, reflecting a higher nitrite formation on Zn_1Sn_1 than on Cu_1Sn_1 at low potentials (Fig. 6a and 6b). On the other hand, nitrite reduction emerges as the rate-limiting step, with the activation energy required decreasing when Sn exclusively acts as H site for reduction reactions on M metals. Note that there is a positive barrier for the pathway of *NO proceeding to NH on Zn-Sn composites, whereas the state of *NO experiences a downhill route to N_2. The small difference in free energies between the parallel *NO to *N and to $*HN_2O$ on Cu-Sn implies its relatively high selectivity toward NH_3 compared to Zn-Sn. This DFT simulation also effectively explains the operando Raman shifts in Fig. 6e and 6f. At elevated cathode potentials, oxide signals like Cu_2O and ZnO noticeably decreased when plated as the sublayers (namely, in Sn_1Cu_1 and Sn_1Zn_1). The adsorption of H^+ on the Sn surface layer creates a more reductive environment for boosting catalytic reactions. Under these conditions, Cu or Zn sites remain in a more metallic state, forming less oxides, for reducing oxygenated nitrogen intermediates.

To evaluate electrochemical NO_3^-RR performance, real nitrate-containing wastewater collected from electroplating effluent was utilized. Results from constant current electrolysis (2 – 10 mA cm^{-2}) on the bimetallic Sn_1Cu_1 and Sn_1Zn_1 electrodes are shown in Fig. 8a – 8c and Fig. 8d – 8f, respectively. As detailed in Table S3, the wastewater contains approximately 500 mg-N L^{-1} NO_3^-, 10 mg-N L^{-1} NO_2^-, and 10 mg-N L^{-1} NH_4^+, along with other major ionic species such as 350 mg L^{-1} Na^+, 600 mg L^{-1} Ca^{2+}, 50 mg L^{-1} Mg^{2+}, 50 mg L^{-1} Cl^-, and 750 mg L^{-1} SO_4^{2-}, contributing to a total ionic strength of around 80 meq L^{-1}. As expected, the observed rate of nitrate removal increases with increasing applied current, with first-order rate constants provided in Fig. 8g. Notably, at low currents of 2–5 mA cm^{-2}, Sn_1Zn_1 produces more nitrite during the 4-hour electrolysis period compared to Sn_1Cu_1. At 10 mA cm^{-2}, however, nitrite formation is significantly inhibited on Sn_1Zn_1, leading to a comparable S_{N2} of 85 %, similar to that on Sn_1Cu_1. This variation in nitrite generation during NO_3^-RR aligns with DFT predictions, which indicate a lower free energy for NO_2(ads) on Cu-Sn than on Zn-Sn bimetallic electrodes.

Sn_1Cu_1 electrode can achieve a similar nitrate removal (>95 %) but with a higher rate (k_{obs} = 1.35 h^{-1}) compared to Sn_1Zn_1 (k_{obs} = 1.17 h^{-1}). Fig. S6 present the performance of monometallic electrodes in the electrolysis of real wastewater at 10 mA cm^{-2}, showing relatively low rate constants of around 0.25 h^{-1}, compared to Sn_1Cu_1 and Sn_1Zn_1 electrodes. During electrolysis at 10 mA cm^{-2}, the energy consumption for reducing nitrate by one order of magnitude (R = 90 %) at time t (h) is calculated:

$$EE/O\ (Wh/m^3) = \frac{E \times I \times t_{90}}{V} = \frac{2.303 \times EI}{V \times k_{obs}} \quad (16)$$

where EE/O refers to electrical energy per order, E and I are voltage and ampere response, 2.303 accounts for the logarithmic factor of 90 % removal (ln(10)), and V is the wastewater volume. The EE/O for

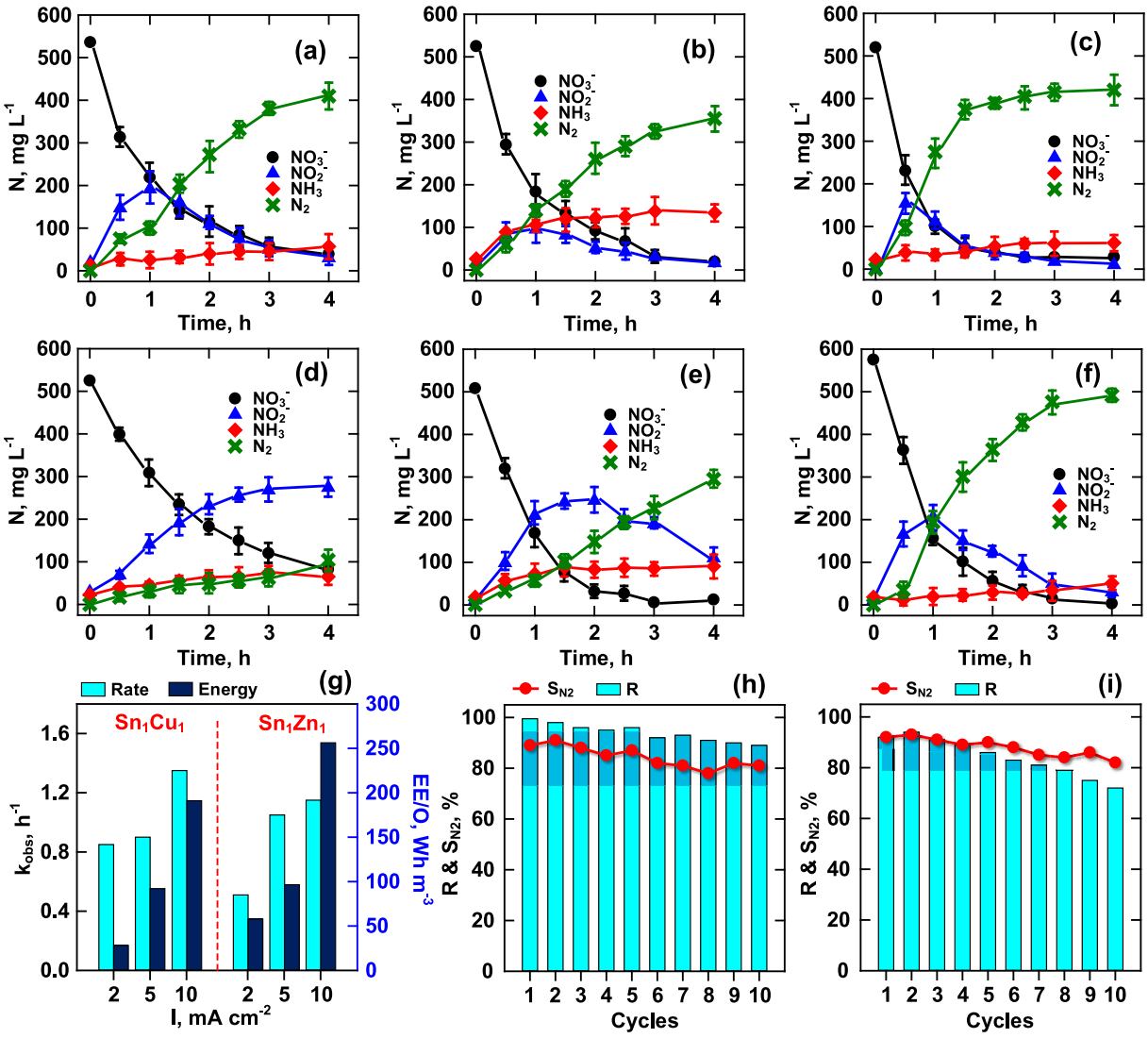

Fig. 8. Constant current electrolysis of nitrate-containing wastewater (NO_3^--N ~ 500 mg L^{-1}, uncontrolled pH) using Sn_1Cu_1 electrode under (a) 2, (b) 5, and (c) 10 mA cm^{-2}, and Sn_1Zn_1 electrode under (d) 2, (e) 5, and (f) 10 mA cm^{-2}, with (g) corresponding observed rate constants and energy consumption. Cycling electrolysis using (h) Sn_1Cu_1 and (i) Sn_1Zn_1 electrodes.

electrochemical denitrification to N_2 reaches 0.19 kWh m^{-3} (or 0.4 kWh kgN^{-1}) on Sn_1Cu_1 and 0.25 kWh m^{-3} (0.5 kWh kgN^{-1}) on Sn_1Zn_1. In terms of electric power utilization, electrochemical NO_3^-RR using M – Sn electrodes demonstrates higher energy efficiency, compared to conventional biological processes, such as bio-denitrification (~2.4 kWh kgN^{-1}) and the ANAMMOX process (1.0 kWh kgN^{-1}) [58]. The cycling performance of NO_3^-RR in wastewater using Sn_1Cu_1 and Sn_1Zn_1 electrodes is depicted in Fig. 8h and 8i, respectively. Over 10 runs of constant current electrolysis (4 h per run), both electrodes maintain N_2 selectivity greater than 80 %, with their removal efficiencies declining by approximately 10 %. To further evaluate the treatability of the real nitrate-containing wastewater, a continuous-flow electrolyzer was assembled to demonstrate the long-term performance of M – Sn electrodes. As schemed in Fig. S7, the electrolyzer consists of an M – Sn/NF cathode and an IrO_2/Ti anode, separated by a 1.5 cm spacer. The flow rate is maintained at 3 mL min^{-1}, resulting in a hydraulic retention time of approximately 50 min. NO_3^-RR results (Fig. S8) indicate that after two or three retention cycles, both Sn_1Cu_1 and Sn_1Zn_1 coatings can achieve a steady nitrate removal exceeding 80 % at 10 mA cm^{-2}, while nitrite and ammonia levels remain below 3 mg-N L^{-1}. The removal efficiency exhibits no significant decline over two days of continuous operation. The above findings confirm the reproducibility of nitrate wastewater remediation and the durability of the bimetallic electrodes.

Following consecutive NO_3^-RR operations, slight metal passivation of these composites is observed, while their crystalline morphology remains intact. As revealed in Fig. 9a – 9c, the divalent Sn(II) dominates in both the used Sn_1Cu_1 and Sn_1Zn_1 electrodes, accounting for over 70 % of the Sn species. Meanwhile, the oxidized Cu and Zn phases also increase to around 70 % in the bimetallic electrodes, compared to less than 60 % in the fresh counterparts (Fig. 3). The metallic surfaces are expected to serve as active sites for the reduction reactions. After long-term electrolysis, an increased presence of oxide states is observed, resulting from electron mediation of adsorbed hydrogen and nitrate species. This phenomenon explains the slight decline in the electrode performance after cycling tests. Elemental mappings in Fig. 9e and 9f show that Sn and O signals are homogeneously distributed across the used Cu and Zn coatings, respectively. Compared to the initial coating compositions in Fig. 2e and 2 k, the atomic ratio of O increases after electrolysis cycles, with noticeable accumulation around Sn clusters. Fig. S9 presents metal concentrations monitored in the electrolyte during cycling tests (Fig. 8h and 8i), which initially remain below tens of μg L^{-1} and decrease to approximately 1 μg L^{-1} after 4 cycles. This outcome indicates the acceptable stability of bimetallic coatings, with dissolved metal levels in the treated solution far below effluent standards set by the USEPA and

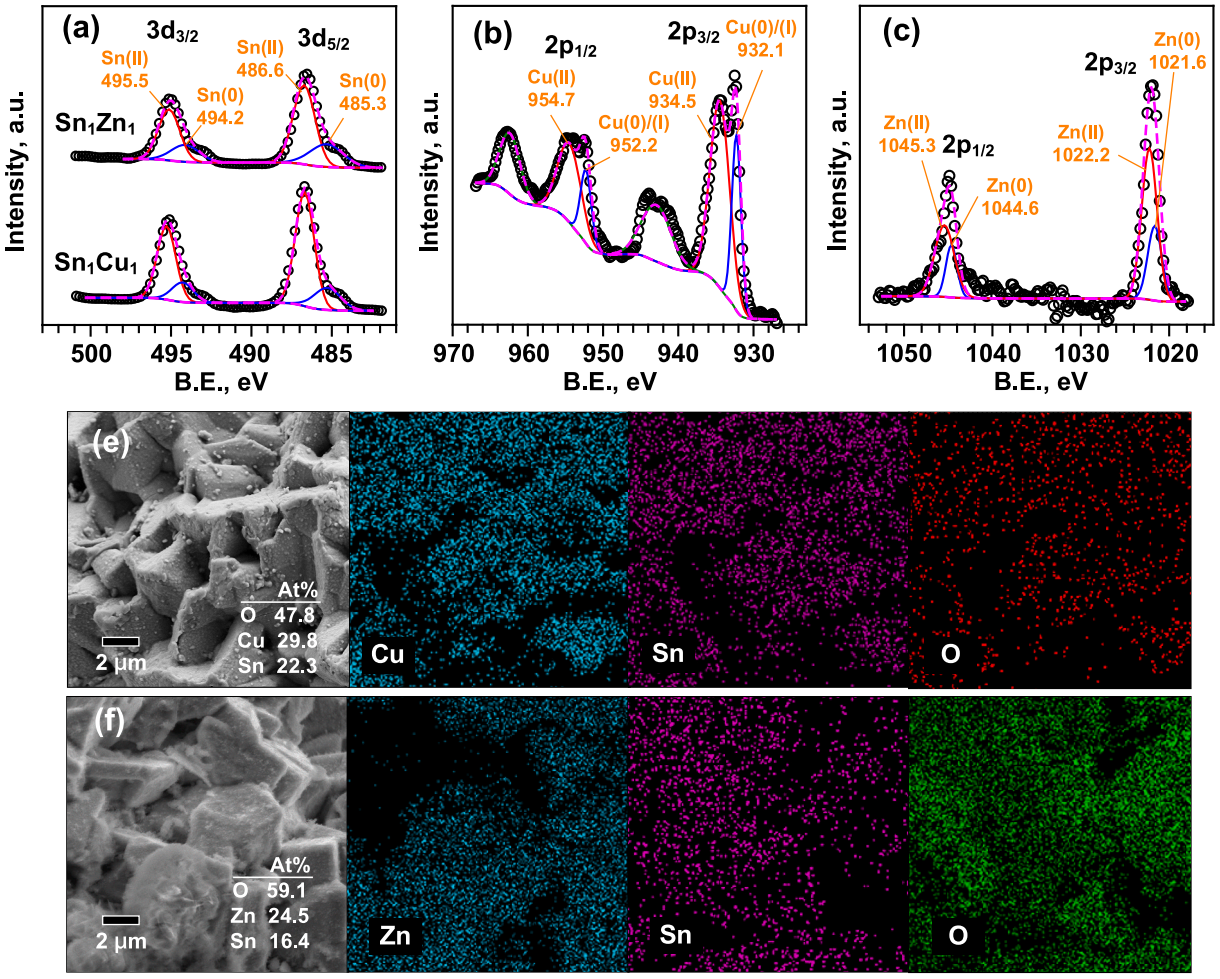

Fig. 9. XPS analyses at (a) Sn 3d, (b) Cu 2p, and (c) Zn 2p orbitals of the surface coatings; SEM and elemental mappings of (e) Sn_1Cu_1 and (f) Sn_1Zn_1 electrodes after cycling electrolysis.

regulations worldwide (Cu = 1.5 mg L^{-1}, Zn = 3.5 mg L^{-1}, Sn = 1 mg L^{-1}). Additionally, Sn_1Zn_1 exhibits lower resistance to leaching compared to Sn_1Cu_1, thus leading to a notable decline in removal efficiency after NO_3^-RR cycles (Fig. 8i). The relatively high Zn loss also explains its reduced ratio in the used electrode, based on EDS analysis (Fig. 2k vs. Fig. 9f). Sn may undergo moderate corrosion during the hydrogenation process even though the composite stability is well maintained after the repeated electrolysis.

While electrochemical NO_3^-RR has been widely studied for ammonia synthesis, achieving selective conversion to N_2 remains challenging, particularly without the assistance of chloride electrolysis. Electroreduction of relatively low nitrate concentrations to non-toxic nitrogen gas emerges as a more economical and eco-friendly solution. Table 1 summarizes recent studies on NO_3^-RR to N_2 using metallic electrodes, with nitrate concentrations typically ranging between 10 – 100 mg-N L^{-1}. The averagely low N_2 selectivity (S_{N2} ~ 50 %) on monometallic electrodes such as Co [59], Fe [60], Sn [25], and Cu [33] can be moderately improved through strategies including organic chelation, carbon substrate, or tuning crystal facet. Bimetallic electrodes frequently employed Cu [61] and Pd [62] as active sites due to their effectiveness in nitrate adsorption and hydrogenation reactions, respectively. Therefore, integrating Cu-Pd in varied topographical configurations [16,56,63–65] has proven to be the best option for NO_3^-RR, leading to N_2 selectivity of up to 80 %. We previously demonstrated that a small amount of Pd NPs decoration (~5%) on PdSn(200) could direct pathways of nitrite to N_2 [19]. In the present work, Sn, in combination with cost-effective non-precious Cu and Zn metals, achieves comparable S_{N2}, while the plating sequence plays a critical role in suppressing ammonia and nitrite formation, respectively. Furthermore, these two bimetallic electrodes are validated for practical nitrate reduction in real wastewater with satisfied stability and reproducibility.

4. Conclusions

On bimetallic electrodes (M – Sn, M = Cu or Zn), the redox couple of M(I)/(II) ⇌ M^0 directly mediates electron transfer for nitrate deoxygenation under cathode polarity. The plating mode critically influences the hydrogenation of nitrogen intermediate and the formation of gaseous N_2. Morphological and capacitive analyses reveal that Sn crystallites plated as surface coatings are uniformly decorated on Cu or Zn base, resulting in an enhanced effective surface area. DFT modelling highlights the positive effect of plating Sn onto M bases, showing a decrease in the activation energy of *NO_2 to *NO step. Moreover, Sn as a surface layer also lowers the energy state of N_2 formation. This prediction well explains the inhibition of NH_3 and NO_2^- formation on bimetallic electrodes with Sn coatings on Cu and Zn sublayers, respectively. Electrochemical NO_3^-RR using a real wastewater containing around 500 mg-N L^{-1} demonstrates the viability of Sn_1Cu_1 and Sn_1Zn_1 electrode in nitrate conversion to N_2 with selectivity exceeding 85 %. Additionally, integrating Sn into the Cu-Sn and Zn-Sn electrodes largely limits metal passivation, as evidenced by stable performance during cycling electrolysis.

Table 1
Summary of metallic electrodes for NO_3^-RR to nitrogen gas.

Electrodes	Synthesis	Properties	Ref.
CoPBA/GO	Prussian blue analogue Co adsorption on graphene oxide	50 mg/L, E = −1.3 V (vs. Ag/AgCl), R = 100 %, S_{N2} = 98 %	[59]
CL-Fe@C	Corchorifolius-like carbon Fe microsphere	100 mg/L, E = −1.3 V (vs. RHE), R = 98 %, S_{N2} = 54 %	[60]
Sn(200)/Ni	Electroplating Sn on Ni foam with BZT surfactant	50 mg/L, I = 20 mA/cm^2, R = 99 %, S_{N2} = 66 %	[25]
Cu_2O/Cu	Electroless plating of Cu on Ni foam	50 mg/L, E = −0.6 (vs. Hg/HgO), R = 42 %, S_{N2} = 55.6 %	[33]
rGO/Fe_1Cu_{15}/CC	$NaBH_4$ reduction of Fe and Cu on carbon cloth	15 mg/L, E = 0.5 V, R = 94 %, S_{N2} = 73 %	[61]
In-Pd/AC	Deposition of In-Pd NPs in activated carbon	50 mg/L, voltage = 1.5 V, R = 96 %, S_{N2} = 91 %	[62]
Pd/Cu	Pd electrodepostion on Cu mesh for 180 s	600 mg/L, I = 0.68 mA/cm^2, R = 99 %, S_{N2} = 86 %	[63]
p-PdCu NC	Partially Cu coating on Pd nanocube	100 mg/L, E = −0.5 V (vs. RHE), R = 95 %, S_{N2} = 89 %	[56]
O1-PdCu/C	Solvothermal PdCu alloy supported on carbon	100 mg/L, E = −0.5 V (vs. RHE), R = 98 %, S_{N2} = 92 %	[64]
Cu-Pd@N-OMC	Pyrolysis of N-Cu–Pd MOFs in ordered mesoporous carbon	100 mg/L, E = −1.3 V (vs. SCE), R = 91 %, S_{N2} = 84 %	[65]
$Pd_{0.27}Cu_{0.73}$/SS	Electroplating Pd on Cu (111)	50 mg/L, I = 3 mA/cm^2, R = 99 %, S_{N2} = 65 %	[16]
Pd_5Sn_{95}	Electroplating Pd on Sn (200)	50 mg/L, I = 20 mA/cm^2, R = 97 %, S_{N2} = 85 %	[19]
Sn_1Cu_1	Layered-plating of Sn on Cu	100 mg/L, E = −1.0 (vs. RHE), R = 82 %, S_{N2} = 90 % Real wastewater, 500 mg/L, I = 10 mA/cm^2, R = 95 %, S_{N2} = 85 %	Present work
Sn_1Zn_1	Layered-plating of Sn on Zn	100 mg/L, E = −1.2 (vs. RHE), R = 88 %, S_{N2} = 92 % Real wastewater, 500 mg/L, I = 10 mA/cm^2, R = 92 %, S_{N2} = 86 %	Present work

CRediT authorship contribution statement

Zhi-Lun Wu: Software, Investigation, Formal analysis, Data curation. **Yu-Jen Shih:** Writing – review & editing, Writing – original draft, Validation, Supervision, Project administration, Investigation, Funding acquisition, Conceptualization. **I-Hsuan Chen:** Visualization, Methodology, Data curation. **Yi-Chun He:** Validation, Methodology, Investigation, Formal analysis. **Chin-Pao Huang:** Conceptualization, Investigation, Methodology, Supervision.

Declaration of competing interest

The authors declare that they have no known competing financial interests or personal relationships that could have appeared to influence the work reported in this paper.

Acknowledgement

The National Science and Technology Council, Taiwan, is appreciated for generous finance support of this research project under Contract No. NSTC 111-2221-E-110-007-MY3.

Appendix A. Supplementary data

Supplementary data to this article can be found online at https://doi.org/10.1016/j.cej.2025.161956.

Data availability

Data will be made available on request.

References

[1] M. Herrmann, M. Taubert, Biogeochemical Cycling of Carbon and Nitrogen in Groundwater—Key Processes and Microbial Drivers, Encyclopedia of Inland Waters (second Edition) 3 (2022) 412–427, https://doi.org/10.1016/B978-0-12-819166-8.00087-6.
[2] S.O. Akinnawo, Eutrophication: Causes, consequences, physical, chemical and biological techniques for mitigation strategies, Environ. Chall. 12 (2023) 100733, https://doi.org/10.1016/j.envc.2023.100733.
[3] C.J. Cheng, Y.T. Kuo, J.W. Chen, G.J. Wei, Y.J. Lin, Probabilistic risk and benefit assessment of nitrates and nitrites by integrating total diet study-based exogenous dietary exposure with endogenous nitrite formation using toxicokinetic modeling, Environ. Intern. 157 (2021) 106807, https://doi.org/10.1016/j.envint.2021.106807.
[4] R. Picetti, M. Deeney, S. Pastorino, M.R. Miller, A. Shah, D.A. Leon, A.D. Dangour, R. Green, Nitrate and nitrite contamination in drinking water and cancer risk: A systematic review with meta-analysis, Environ. Res. 210 (2022) 112988, https://doi.org/10.1016/j.envres.2022.112988.
[5] K.A.N. Berthe, M. Kamagate, Y.K. Marthe, G.D. Lancine, Spatial and temporal assessment of health risks associated with exposure to nitrates from shallow well water in West Africa, J. Hazard. Mater. Adv. 10 (2023) 100323, https://doi.org/10.1016/j.hazadv.2023.100323.
[6] R.C. Scholes, M.A. Vega, J.O. Sharp, D.L. Sedlak, Nitrate removal from reverse osmosis concentrate in pilot-scale open-water unit process wetlands, Environ. Sci.: Water Res. Technol. 7 (2021) 650–661, https://doi.org/10.1039/D0EW00911C.
[7] J.C. Akunna, C. Bizeau, R. Moletta, Nitrate and nitrite reductions with anaerobic sludge using various carbon sources: Glucose, glycerol, acetic acid, lactic acid and methanol, Water Res. 27 (1993) 1303–1312, https://doi.org/10.1016/0043-1354(93)90217-6.
[8] S. Garcia-Segura, M. Lanzarini-Lopes, K. Hristovski, P. Westerhoff, Electrocatalytic reduction of nitrate: Fundamentals to full-scale water treatment applications, Appl. Catal. B: Environ. 236 (2018) 546–568, https://doi.org/10.1016/j.apcatb.2018.05.041.
[9] D. Reyter, Electrochemical Reduction of Nitrate. In: Kreysa, G., Ota, Ki., Savinell, R. F. (eds) Encyclopedia of Applied Electrochemistry. Springer, New York, NY, https://doi.org/10.1007/978-1-4419-6996-5_135.
[10] M.A. Mushtaq, A. Kumar, W. Liu, Q. Ji, Y. Deng, G. Yasin, A. Saad, W. Raza, J. Zhao, S. Ajmal, Y. Wu, M. Ahmad, N.R. Lashari, Y. Wang, T. Li, S. Sun, D. Zheng, Y. Luo, X. Cai, A Metal Coordination Number Determined Catalytic Performance in Manganese Borides for Ambient Electrolysis of Nitrogen to Ammonia, *Adv. Mater.* 36 (2024) 2313086, https://doi.org/10.1002/adma.202313086.
[11] X. Fan, C. Liu, X. He, Z. Li, L. Yue, W. Zhao, J. Li, Y. Wang, T. Li, Y. Luo, D. Zheng, S. Sun, Q. Liu, L. Li, W. Chu, F. Gong, B. Tang, Y. Yao, X. Sun, Efficient Electrochemical Co-Reduction of Carbon Dioxide and Nitrate to Urea with High Faradaic Efficiency on Cobalt-Based Dual-Sites, Adv. Mater. 36 (2024) 2401221, https://doi.org/10.1002/adma.202401221.
[12] G.B. Truong, H.T. Duong, L.D. Vu, T.T.H. Hoang, Highly Efficient Electrochemical Nitrate and Nitrogen Reduction to Ammonia under Ambient Conditions on Electrodeposited Cu-Nanosphere Electrode, Eur. J. Inorg. Chem. 26 (2023) e202300371, https://doi.org/10.1002/ejic.202300371.
[13] M.M. Islam, S.M.A. Nayem, S.S. Shah, M.Z. Islam, M.A. Aziz, A.J.S. Ahammad, Electrochemical Selective Nitrate Reduction: Pathways to Nitrogen and Ammonia Production, Chem. Rec. (2024) e202400206, https://doi.org/10.1002/tcr.202400206.
[14] G.A. Cerrón-Calle, A.S. Fajardo, C.M. Sánchez-Sánchez, S. Garcia-Segura, Highly reactive Cu-Pt bimetallic 3D-electrocatalyst for selective nitrate reduction to ammonia, Appl. Catal. B: Environ. 302 (2022) 120844, https://doi.org/10.1016/j.apcatb.2021.120844.
[15] J. Liang, Z. Li, L. Zhang, X. He, Y. Luo, D. Zheng, Y. Wang, T. Li, H. Yan, B. Ying, S. Sun, Q. Liu, M.S. Hamdy, B. Tang, X. Sun, Advances in ammonia electrosynthesis from ambient nitrate/nitrite reduction, Chem 9 (2023) 1768–1827, https://doi.org/10.1016/j.chempr.2023.05.037.
[16] Y.J. Shih, Z.L. Wu, C.Y. Lin, Y.H. Huang, C.P. Huang, Manipulating the crystalline morphology and facet orientation of copper and copper-palladium nanocatalysts supported on stainless steel mesh with the aid of cationic surfactant to improve the electrochemical reduction of nitrate and N2 selectivity, Appl. Catal. B: Environ. 273 (2020) 119053, https://doi.org/10.1016/j.apcatb.2020.119053.
[17] T. Xie, X. He, L. He, K. Dong, Y. Yao, Z. Cai, X. Liu, X. Fan, T. Li, D. Zheng, S. Sun, L. Li, W. Chu, A. Farouk, M.S. Hamdy, C. Xu, Q. Kong, X. Sun, CoSe2 nanowire array enabled highly efficient electrocatalytic reduction of nitrate for ammonia synthesis, Chin. Chem. Let. 35 (2024) 110005, https://doi.org/10.1016/j.cclet.2024.110005.
[18] Y.J. Shih, Z.L. Wu, Y.C. He, Tuning transition metals layered-electroplated on bimetallic MxCu1-x crystallites (M = Fe, Co, Ni, and Zn) to boost ammonia yield in

electrocatalytic reduction of nitrate wastewaters, J. Hazard. Mater. 477 (2024) 135276, https://doi.org/10.1016/j.jhazmat.2024.135276.
[19] Z.L. Wu, Y.J. Shih, Bimetallic palladium-tin nanoclusters, PdSn(200) and PdSn (101), templated with cationic surfactant for electrochemical denitrification toward N2 and NH4+ selectivity, Chem. Eng. J. 433 (2022) 133852, https://doi.org/10.1016/j.cej.2021.133852.
[20] I. Katsounaros, D. Ipsakis, C. Polatides, G. Kyriacou, Efficient electrochemical reduction of nitrate to nitrogen on tin cathode at very high cathodic potentials, Electrochim. Acta 52 (2006) 1329–1338, https://doi.org/10.1016/j.electacta.2006.07.034.
[21] K.W. Kim, S.M. Kim, Y.H. Kim, E.H. Lee, K.Y. Jee, Sn Stability of Sn-Modified Pt Electrode for Reduction of Nitrate, J. Electrochem. Soc. 154 (2007) E145, https://doi.org/10.1149/1.2769286.
[22] G. Tokazhanov, E. Ramazanova, S. Hamid, S. Baec, W. Lee, Advances in the catalytic reduction of nitrate by metallic catalysts for high efficiency and N2 selectivity: A review, Chem. Eng. J. 384 (2020) 123252, https://doi.org/10.1016/j.cej.2019.123252.
[23] W. He, J. Zhang, S. Dieckhöfer, S. Varhade, A.C. Brix, A. Lielpetere, S. Seisel, J.R. C. Junqueira, W. Schuhmann, Splicing the active phases of copper/cobalt-based catalysts achieves high-rate tandem electroreduction of nitrate to ammonia, Nat. Commun. 13 (2022) 1129, https://doi.org/10.1038/s41467-022-28728-4.
[24] O.Q. Carvalho, S.R.S. Jones, A.E. Berninghaus, R.F. Hilliard, T.S. Radniecki, K. A. Stoerzinger, Role of oxide support in electrocatalytic nitrate reduction on Cu, Electrochem Sci Adv. 4 (2024) e2100201, https://doi.org/10.1002/elsa.202100201.
[25] Y.J. Shih, Z.L. Wu, Electroplating of surfactant-modified tin catalyst over a nickel foam electrode (Sn/Ni) for selective N2 yield from nitrate reduction as affected by Sn(200) and Sn(101) crystal facets, Appl. Catal. B: Environ. 285 (2021) 119784, https://doi.org/10.1016/j.apcatb.2020.119784.
[26] M.G. Park, D.H. Lee, H. Jung, J.H. Choi, C.M. Park, Sn-Based Nanocomposite for Li-Ion Battery Anode with High Energy Density, Rate Capability, and Reversibility, ACS Nano 12 (3) (2018) 2955–2967, https://doi.org/10.1021/acsnano.8b00586.
[27] Y.A. Shao, Y.T. Chen, P.Y. Chen, Cu and CuPb electrodes prepared via potentiostatic electrodeposition from metal oxides in hydrophobic protic amide-type ionic liquid/water mixture under ambient air for nonenzymatic nitrate reduction, Electrochim. Acta 313 (2019) 488–496, https://doi.org/10.1016/j.electacta.2019.05.057.
[28] I. Kurmanbayeva, L. Rakhymbay, K. Korzhynbayeva, A. Adi, D. Batyrbekuly, A. Mentbayeva, Z. Bakenov, Tetrapropylammonium Hydroxide as a Zinc Dendrite Growth Suppressor for Rechargeable Aqueous Battery, Front. Energy Res. 8 (2020) 599009, https://doi.org/10.3389/fenrg.2020.599009.
[29] X. Kong, H. Wu, K. Lu, X. Zhang, Y. Zhu, H. Lei, Galvanic Replacement Reaction: Enabling the Creation of Active Catalytic Structures, ACS Appl. Mater. Interf. 15 (2023) 41205–41223, https://doi.org/10.1021/acsami.3c08922.
[30] I. Borbáth, I. Bakos, Z. Pászti, G.P. Szijjártó, A. Tompos, Design of SnPt/C cathode electrocatalysts with optimized Sn/Pt surface composition for potential use in Polymer Electrolyte Membrane Fuel Cells, Catal. Today 366 (2021) 20–30, https://doi.org/10.1016/j.cattod.2020.06.029.
[31] J. de Almeida, M.S. Pacheco, J.F. de Brito, Contribution of CuxO distribution, shape and ratio on TiO2 nanotubes to improve methanol production from CO2 photoelectroreduction, J. Solid State Electrochem. 24 (2020) 3013–3028, https://doi.org/10.1007/s10008-020-04739-3.
[32] Y. Qu, G. Zoppi, N.S. Beattie, The role of nanoparticle inks in determining the performance of solution processed $Cu_2ZnSn(S,Se)_4$ thin film solar cells, Prog. Photovolt: Res. Appl. 24 (2016) 836–845, https://doi.org/10.1002/pip.2756.
[33] Y.J. Shih, Z.L. Wu, Y.H. Huang, C.P. Huang, Electrochemical nitrate reduction as affected by the crystal morphology and facet of copper nanoparticles supported on nickel foam electrodes (Cu/Ni), Chem. Eng. J. 383 (2020) 123157, https://doi.org/10.1016/j.cej.2019.123157.
[34] E. Murphy, Y. Liu, I. Matanovic, M. Rüscher, Y. Huang, A. Ly, S. Guo, W. Zang, X. Yan, A. Martini, J. Timoshenko, B.R. Cuenya, I.V. Zenyuk, X. Pan, E.D. Spoerke, P. Atanassov, Elucidating electrochemical nitrate and nitrite reduction over atomically-dispersed transition metal sites, Nat. Commun. 14 (2023) 4554, https://doi.org/10.1038/s41467-023-40174-4.
[35] K.M. Lodaya, B.Y. Tang, R.P. Bisbey, S. Weng, K.S. Westendorff, W.L. Toh, J. Ryu, Y. Román-Leshkov, Y. Surendranath, An electrochemical approach for designing thermochemical bimetallic nitrate hydrogenation catalysts, Nat. Catal. 7 (2024) 262–272, https://doi.org/10.1038/s41929-023-01094-0.
[36] J.G. Velasco, Determination of Standard Rate Constants for ElectrochemicalIrreversible Processes from Linear Sweep Voltammograms, Electroanalysis 9 (1997) 880–882, https://doi.org/10.1002/elan.1140091116.
[37] R.L. Donkers, F. Maran, D.D.M. Wayner, M.S. Workentin, Kinetics of the Reduction of Dialkyl Peroxides. New Insights into theDynamics of Dissociative Electron Transfer, J. Am. Chem. Soc. 121 (1999) 7239–7248, https://doi.org/10.1021/ja9906148.
[38] A.R.C. Bredar, A.L. Chown, A.R. Burton, B.H. Farnum, Electrochemical Impedance Spectroscopy of Metal Oxide Electrodes for Energy Applications, ACS Appl. Energy Mater. 3 (2020) 66–98, https://doi.org/10.1021/acsaem.9b01965.
[39] R. Ahmad, N. Tripathy, M.S. Ahn, K.S. Bhat, T. Mahmoudi, Y. Wang, J.Y. Yoo, D. W. Kwon, H.Y. Yang, Y.B. Hahn, Highly Efficient Non-Enzymatic Glucose Sensor Based on CuO Modified Vertically-Grown ZnO Nanorods on Electrode, Sci. Rep. 7 (2017) 5715, https://doi.org/10.1038/s41598-017-06064-8.
[40] A. Allagui, T.J. Freeborn, A.S. Elwakil, B.J. Maundy, Reevaluation of Performance of Electric Double-layer Capacitors from Constant-current Charge/Discharge and Cyclic Voltammetry, Sci. Rep. 6 (2016) 38568, https://doi.org/10.1038/srep38568.
[41] D. Cheng, Z. Wei, Z. Zhang, P. Broekmann, A.N. Alexandrova, P. Sautet, Restructuring and Activation of Cu(111) under Electrocatalytic Reduction Conditions, Angew. Chem. Int. Ed. 62 (2023) e202218575, https://doi.org/10.1002/anie.202218575.
[42] P. Pal, J.M. Ting, S. Agarwal, T. Ichikawa, A. Jain, The Catalytic Role of D-block Elements and Their Compounds for Improving Sorption Kinetics of Hydride Materials: A Review, Reactions 2 (3) (2021) 333–364, https://doi.org/10.3390/reactions2030022.
[43] M. Liu, L.Y.S. Lee, K.Y. Wong, Highly Efficient Electrocatalytic Water Splitting, Handbook of Nanomaterials and Nanocomposites for Energy and Environmental Applications, Springer, Cham. (2021), https://doi.org/10.1007/978-3-030-36268-3_131.
[44] L. Wang, W. Huang, W. Guo, Z.H. Guo, C. Chang, L. Gao, X. Pu, Sn Alloying to Inhibit Hydrogen Evolution of Zn MetalAnode in Rechargeable Aqueous Batteries, Adv. Funct. Mater. 32 (2022) 2108533, https://doi.org/10.1002/adfm.202108533.
[45] T. Ito, F.W. Seidel, X. Jin, K. Nozaki, TEMPO as a Hydrogen Atom Transfer Catalyst for Aerobic Dehydrogenation of Activated Alkanes to Alkenes, J. Org. Chem. 87 (19) (2022) 12733–12740, https://doi.org/10.1021/acs.joc.2c01302.
[46] A. Elgendy, H. Nady, M.M. El-Rabieib, A.A. Elhenawy, Understanding the adsorption performance of two glycine derivatives as novel and environmentally safe anti-corrosion agents for copper in chloride solutions: experimental, DFT, and MC Studies, RSC Adv. 9 (2019) 42120–42131, https://doi.org/10.1039/C9RA08617J.
[47] Y. Wang, A. Xu, Z. Wang, L. Huang, J. Li, F. Li, J. Wicks, M. Luo, D.H. Nam, C. S. Tan, Y. Ding, J. Wu, Y. Lum, C.T. Dinh, D. Sinton, G. Zheng, E.H. Sargent, Enhanced Nitrate-to-Ammonia Activity on Copper–Nickel Alloys via Tuning of Intermediate Adsorption, J. Am. Chem. Soc. 142 (2020) 5702–5708, https://doi.org/10.1021/jacs.9b13347.
[48] Y.T. Chiu, C.H. Lin, J. Lee, K.Y. Andrew Lin, Reduction of nitrate to nitrite in water by acid-washed zero-valent zinc, Sep. Sci. Technol. 55 (2020) 761–770, https://doi.org/10.1080/01496395.2019.1577263.
[49] R. Chellappa, D. Dattelbaum, L. Daemen, Z. Liu, High pressure spectroscopic studies of hydrazine (N_2H_4), J. Phys. Conf. Ser. 500 (2014) 052008, https://doi.org/10.1088/1742-6596/500/5/052008.
[50] A. Vázquez-López, D. Maestre, J. Ramírez-Castellanos, A. Cremades, In Situ Local Oxidation of SnO Induced by Laser Irradiation: A Stability Study, Nanomaterials 11 (2021) 976, https://doi.org/10.3390/nano11040976.
[51] P. Pandey, M.R. Parra, F.Z. Haque, R. Kurchania, Effects of annealing temperature optimization on the efficiency of ZnO nanoparticles photoanode based dye sensitized solar cells, J Mater Sci: Mater Electron 28 (2017) 1537–1545, https://doi.org/10.1007/s10854-016-5693-9.
[52] J.F. van Staden, M.A. Makhafola, D. de Waal, Kinetic Study of the Decomposition of Nitrite to Nitrate in Acid Samples Using Raman Spectroscopy, Appl. Spec. 50 (8) (1996) 991–994, https://doi.org/10.1366/0003702963905303.
[53] A. Prajapat, M. Aslam, I. Rana, K.R. Ranjan, P. Singh, C. Verma, A. AlFantazi, K. Kumari, Computational supported experimental insights in adsorption of Congo Red using ZnO/doped ZnO in aqueous solution, Sci. Rep. 14 (2024) 27189, https://doi.org/10.1038/s41598-024-77619-9.
[54] D.Y. Shin, D.H. Lim, DFT investigation into efficient transition metal single-atom catalysts supported on N-doped graphene for nitrate reduction reactions, Chem. Eng. J. 468 (2023) 143466, https://doi.org/10.1016/j.cej.2023.143466.
[55] S. Zhang, J. Wu, M. Zheng, X. Jin, Z. Shen, Z. Li, Y. Wang, Q. Wang, X. Wang, H. Wei, J. Zhang, P. Wang, S. Zhang, L. Yu, L. Dong, Q. Zhu, H. Zhang, J. Lu, Fe/Cu diatomic catalysts for electrochemical nitrate reduction to ammonia, Nat. Commun. 14 (2023) 3634, https://doi.org/10.1038/s41467-023-39366-9.
[56] J. Lim, Y. Chen, D.A. Cullen, S.W. Lee, T.P. Senftle, M.C. Hatzell, PdCu Electrocatalysts for Selective Nitrate and Nitrite Reduction to Nitrogen, ACS Catal. 13 (2023) 87–98, https://doi.org/10.1021/acscatal.2c04841.
[57] S. Subhadarshini, M. Pumera, Single Atom Catalyst for Nitrate-to-Ammonia Electrochemistry, Small 2403515 (2024), https://doi.org/10.1002/smll.202403515.
[58] M. Figueroa, J.R. Vázquez-Padín, A. Mosquera-Corral, J.L. Campos, R. Méndez, Is the CANON reactor an alternative for nitrogen removal from pre-treated swine slurry? Biochem. Eng. J. 65 (2012) 23–29, https://doi.org/10.1016/j.bej.2012.03.008.
[59] B. Xu, Z. Chen, G. Zhang, Y. Wang, On-Demand Atomic Hydrogen Provision by Exposing Electron-Rich Cobalt Sites in an Open-Framework Structure toward Superior Electrocatalytic Nitrate Conversion to Dinitrogen, Environ. Sci. Technol. 56 (2022) 614–623, https://doi.org/10.1021/acs.est.1c06091.
[60] L. Su, D. Han, G. Zhu, H. Xu, W. Luo, L. Wang, W. Jiang, A. Dong, J. Yang, Tailoring the Assembly of Iron Nanoparticles in Carbon Microspheres toward High-Performance Electrocatalytic Denitrification, Nano Lett. 19 (8) (2019) 5423–5430, https://doi.org/10.1021/acs.nanolett.9b01925.
[61] W. Li, Q. Yin, C. Liu, S. Yang, D. Jin, X. Wang, L. Song, Fabrication of FeCu/CC Composite for Efficient Removal of Nitrate for Aqueous Solution Via Electrochemical Reduction Process, ChemCatChem 16 (2024) e202401017, https://doi.org/10.1002/cctc.202401017.
[62] T.K. Rogers, S. Guo, L. Arrazolo, S. Garcia-Segura, M.S. Wong, R. Verduzco, Catalytic Capacitive Deionization for Adsorption and Reduction of Aqueous Nitrate, ACS ES&T Water 1 (10) (2021) 2233–2241, https://doi.org/10.1021/acsestwater.1c00195.
[63] K.L. Chen, M.S. Ahmad, C.L. Chen, Enhanced nitrate reduction over functionalized Pd/Cu electrode with tunable conversion to nitrogen and sodium hydroxide

recovery, Sci. Total Environ. 869 (2023) 161849, https://doi.org/10.1016/j.scitotenv.2023.161849.
[64] J. Lim, D.A. Cullen, E. Stavitski, S.W. Lee, M.C. Hatzell, Atomically Ordered PdCu Electrocatalysts for Selective and Stable Electrochemical Nitrate Reduction, ACS Energy Lett. 8 (2023) 4746–4752, https://doi.org/10.1021/acsenergylett.3c01672.
[65] J. Wang, W. Teng, L. Ling, J. Fan, W. Zhang, Zi. Deng, Nanodenitrification with bimetallic nanoparticles confined in N-doped mesoporous carbon, Environ. Sci.: Nano 7 (2020) 1496, .